CRYSTAL GROWTH & DESIGN

pubs.acs.org/crystal

Article

Anisotropic Etching Patterns in 2D Cr_5Te_8 Nanosheets and Their Arduous Saturation Magnetization

Hanxiang Wu, Zuoquan Tan, Zhaxi Suonan, Shanshan Chen, Rui Xu, Wei Ji, Zhihai Cheng, and Fei Pang*

Cite This: https://doi.org/10.1021/acs.cgd.5c00094

Read Online

ACCESS | Metrics & More | Article Recommendations

ABSTRACT: Although 2D self-intercalated Cr_5Te_8 has been successfully synthesized via chemical vapor deposition (CVD), its etching behavior remains largely unexplored. Etching, as the inverse process of material growth, is essential for understanding growth mechanisms and fabricating nanosheet patterns. Herein, we explore the anisotropic etching of 2D Cr_5Te_8 assisted by an excess Te supply. The etching process initiates from both the surface and the edge, creating distinct holes and nanoribbons with triangular or hexagonal shapes. To the best of our knowledge, this is the first report on controllable anisotropic etching patterns in 2D Cr_5Te_8. Furthermore, magnetic measurements reveal ferromagnetism in the etched nanosheets with a Curie temperature (T_C) of 164 K, slightly lower than that of the unetched nanosheets. The etched nanosheets exhibit an enhanced saturated magnetic field of 38.5 kOe, approximately 3.2 times that of the unetched nanosheets. This enhancement in the saturated magnetic field is attributed to the pattern-induced strengthening of the reentrant stray field. This study offers a new direction for preparing patterned 2D materials and opens a novel avenue for modulating 2D magnetism.

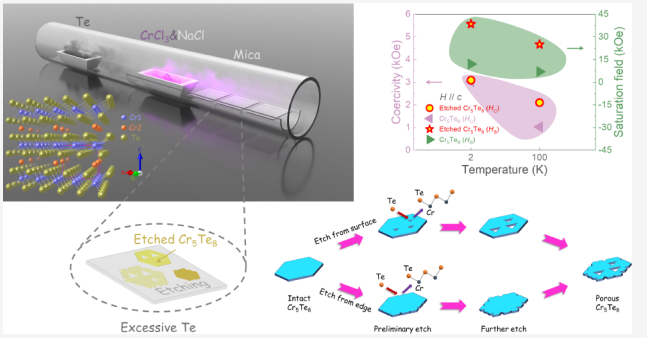

INTRODUCTION

Due to their exceptional electrical,[1,2] photoelectrical,[3,4] and magnetic properties,[5−7] two-dimensional (2D) magnetic materials have attracted considerable attention for their potential in diverse applications. Among these, self-intercalated 2D chromium telluride (Cr_xTe_y) stands out due to its diverse thickness-dependent magnetism and self-intercalated phases, offering significant prospects for fundamental studies and spintronic device applications.[8−20] Notably, the 2D Cr_5Te_8 nanosheet has been reported to exhibit ferromagnetism with pronounced out-of-plane spin polarization, facilitated by strong interlayer magnetic coupling.[21−29] Additionally, magnetic force microscopy (MFM) has revealed magnetic bubbles and thickness-dependent labyrinthine domains in Cr_5Te_8 nanosheets, underscoring the transition in the dominant role of ferromagnetism from dipolar interactions to magnetic anisotropy in the 2D regime.[21]

Despite the successful synthesis of 2D Cr_5Te_8 via chemical vapor deposition (CVD), the growth mechanism of self-intercalated 2D Cr_5Te_8 remains incompletely understood.[21−26] From a microscopic perspective, etching is commonly perceived as the inverse process of growth.[30−33] Hence, understanding the etching process of materials is essential for gaining insight into their growth mechanisms. Furthermore, etching is widely recognized as a top-down approach for constructing specific patterns, potentially leading to the emergence of unique properties due to symmetry alterations in the material.[32] Previous research on 2D material etching has focused on graphene,[34] hexagonal boron nitride (h-BN),[35] transition metal dichalcogenides (TMDs),[32,36,37] and metal monochalcogenides,[30] while the self-intercalated structure of Cr_5Te_8, where intercalated Cr atoms chemically bond with Te atoms, suggests distinct growth and etching mechanisms compared to these materials. However, research on the etching behavior of self-intercalated materials during the CVD process is still in its nascent stages, lacking both theoretical guidance and experimental evidence.[31,33] Therefore, investigating the etching behavior of 2D Cr_5Te_8 is crucial for a profound understanding of the etching and growth mechanisms of self-intercalated materials, as well as for tuning emergent 2D magnetism.

Herein, we fabricated Cr_5Te_8 nanosheets with anisotropic etching holes and nanoribbons. Under excess Te supply,

Received: January 21, 2025
Revised: July 31, 2025
Accepted: July 31, 2025

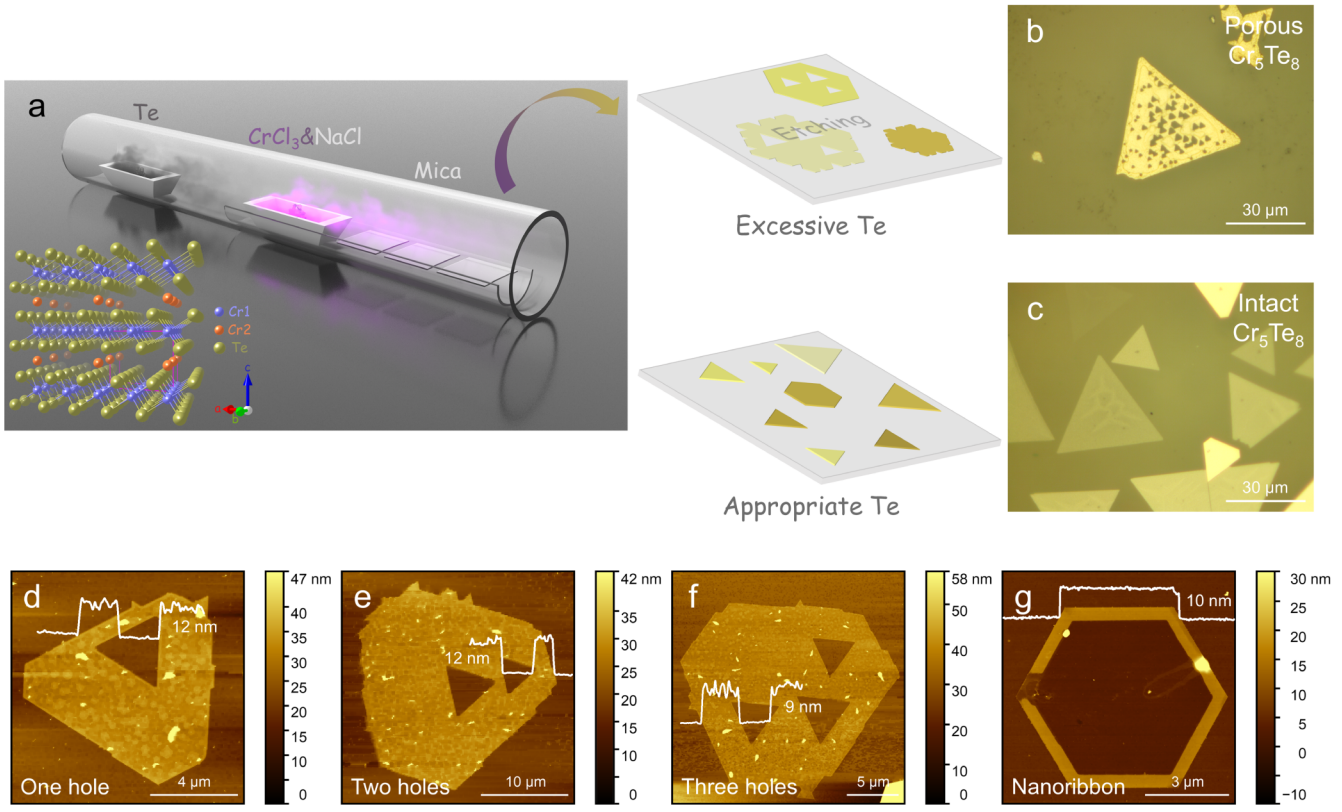

Figure 1. Growth method and morphology in etched Cr_5Te_8. (a) Schematic diagram illustrating the one-step CVD growth of etched Cr_5Te_8 nanosheets. The inset depicts the crystal structure (side view) of Cr_5Te_8. (b,c) Typical OM images of Cr_5Te_8 grown on mica substrates with excessive (b) and appropriate (c) Te powder. (d–f) Typical AFM topographies of etched Cr_5Te_8 nanosheets with 1 hole (d), 2 holes (e), and 3 holes (f), respectively. (g) AFM topography of the resulting Cr_5Te_8 nanoribbons after etching.

Cr_5Te_8 nanosheets undergo anisotropic etching, resulting in well-defined patterns, such as triangular and hexagonal holes on the nanosheets. Furthermore, by precisely adjusting the Te source, Cr_5Te_8 nanosheets were etched into nanoribbons. The etching process was initiated from the surface and the edge. Although a similar etching process by excess chalcogen precursors was reported in the CVD growth of MoS_2 nanosheets, excess sulfur etching only reduced edge length and did not form pattern structure.[36] To the best of our knowledge, this is the first experimental demonstration of controllable etching in 2D Cr_5Te_8 nanosheets. Optical microscopy (OM), atomic force microscopy (AFM), X-ray diffraction (XRD), X-ray photoelectron spectroscopy (XPS), scanning electron microscopy (SEM) coupled with energy-dispersive spectroscopy (EDS), and Raman spectroscopy confirmed the high crystallinity, accurate composition, and structure of etched Cr_5Te_8 nanosheets. Additionally, the magnetic property measurement system (MPMS) revealed that etched Cr_5Te_8 nanosheets exhibit ferromagnetism with a Curie temperature (T_C) of 164 K. Notably, these etched nanosheets demonstrated an enhanced saturated magnetic field of up to 38.5 kOe, possibly attributed to the increased edge proportion, which strengthens the reentrant stray field of the saturated magnetic domains. This study provides crucial insights into the multifaceted etching behavior of Cr_5Te_8, offering a novel approach for modulating the magnetism of 2D materials and serving as an important experimental reference for understanding the etching behavior and emergent properties of other self-intercalated materials during the CVD process.

MATERIAL AND METHODS

Growth of Etched Cr_5Te_8. The growth of etched Cr_5Te_8 nanosheets was conducted in a dual-zone tubular furnace equipped with a 1-in. diameter quartz tube by atmospheric pressure CVD. Te powder (0.5−1 g, Alfa Aesar, 99.99% purity) was positioned in the first temperature zone (700 °C), while a mixture of $CrCl_3$ (4 mg, Alfa Aesar, 99.9% purity) as the Cr precursor and NaCl (1.5 mg, Alfa Aesar, 99.99% purity) as the cosolvent was placed in the second temperature zone (850 °C) inside the quartz tube. Freshly cleaved fluorophlogopite mica ($KMg_3AlSi_3O_{10}F_2$) substrates were positioned adjacent to the $CrCl_3$ powder. Prior to growth, the quartz tube underwent vacuuming and purging with Ar gas twice to eliminate oxygen and moisture residues. A mixture of 145 sccm Ar and 5 sccm H_2 was used to transport vapor species to the substrates, and the growth process lasted for about 10 min.

Transfer of Etched Cr_5Te_8. Etched Cr_5Te_8 nanosheets on mica were transferred to SiO_2/Si substrates by using polystyrene (PS) as a medium for further characterization. Briefly, the etched Cr_5Te_8 grown on mica was coated with a PS solution and baked on a hot plate at 60 °C for 30 min to enhance adhesion between the nanosheets and PS. Subsequently, the PS/etched Cr_5Te_8/mica was immersed in deionized water to separate the PS/etched Cr_5Te_8 from the mica. The PS/etched Cr_5Te_8 was then transferred onto SiO_2/Si substrates and baked again at 60 °C for 30 min. Finally, the PS was removed by using anisole.

Characterization of Etched Cr_5Te_8. The morphology and thickness of the etched Cr_5Te_8 nanosheets were characterized using OM (6XB-PC, Shang Guang) and AFM (Dimension ICON, Bruker). The phase structure of the etched Cr_5Te_8 was analyzed by XRD (D8 ADVANCE, Bruker). XPS (ESCALAB 250Xi, Thermo Fisher Scientific) was used to analyze the binding energies. The elemental composition and distribution were evaluated using SEM (NOVA NANOSEM450, FEI) equipped with EDS (X-MaxN 50 mm^2, Oxford

https://doi.org/10.1021/acs.cgd.5c00094
Cryst. Growth Des. XXXX, XXX, XXX−XXX

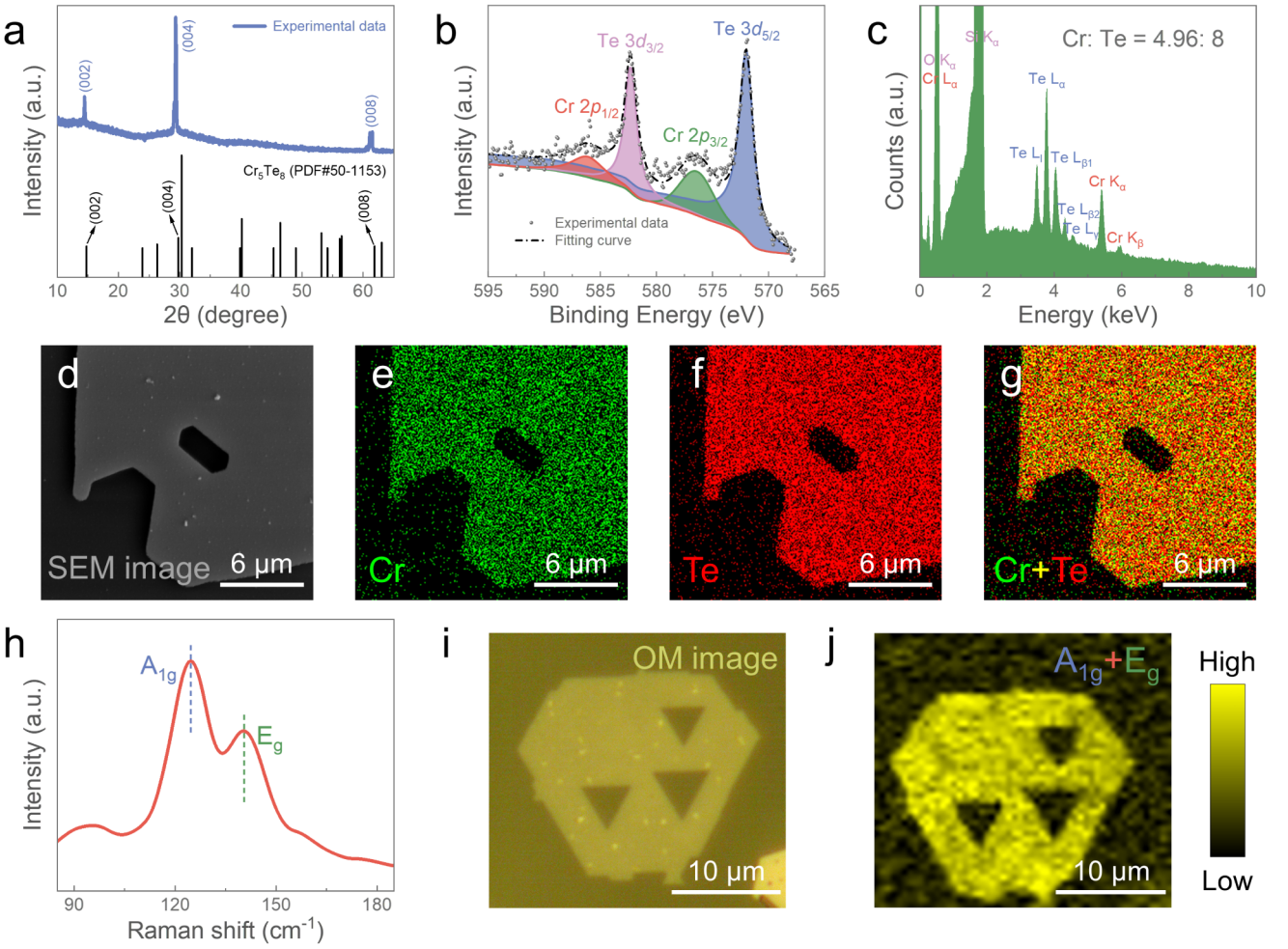

Figure 2. Structural and compositional characterization of etched Cr_5Te_8. (a) XRD patterns of etched Cr_5Te_8 nanosheets transferred to the SiO_2/Si substrate (top) and the standard Cr_5Te_8 crystal from the PDF card (bottom). (b) XPS of etched Cr_5Te_8 nanosheets. (c) EDS of etched Cr_5Te_8 nanosheets. (d–g) SEM image (d) and the corresponding EDS mapping of the Cr element (e), Te element (f), and an overlay of Cr and Te elements (g) of a representative etched Cr_5Te_8 nanosheet. (h) Raman spectrum of an individual etched Cr_5Te_8 nanosheet. (i,j) OM image (i) and the corresponding Raman mapping of an overlay of A_{1g} and E_g modes (j) of a representative etched Cr_5Te_8 nanosheet.

Instruments). Raman spectroscopy was employed to identify vibrational modes using confocal Raman microscopy (alpha300 R, WITec).

The T_C and magnetic hysteresis loops were measured by MPMS (MPMS3, Quantum Design), which was used to measure the magnetic properties of etched Cr_5Te_8 on mica, including saturated magnetic field values. The temperature-dependent magnetic moments (M–T) were measured between 1.8 and 400 K through zero-field cooling (ZFC) and field cooling (FC) processes with an additional magnetic field of 1 kOe perpendicular to the *ab*-plane. Field-dependent magnetizations (M–H) were carried out with the applied field ranging from −70,000 Oe to +70,000 Oe perpendicular to the *ab*-plane at 2 and 100 K.

RESULTS AND DISCUSSION

The one-step CVD growth process used to synthesize 2D Cr_5Te_8 nanosheets with etched patterns is depicted in Figure 1a. Within a dual-zone tubular furnace, Te powder is positioned in the first temperature zone, while a mixture of $CrCl_3$ and NaCl powders is placed in the second temperature zone inside the quartz tube. The mica substrates are positioned in proximity to the mixture of $CrCl_3$ and NaCl powders. Etching and growth are complementary processes. The two processes compete during the growth of the 2D crystal.[30] Therefore, the dominant role between etching and growth changes with the amount of Te precursors, which shifts from growth to etching as the amount of Te precursors increases. According to the amount of Te precursors, we define the amount of Te powder and its corresponding vapor temperature for unetched Cr_5Te_8 nanosheet synthesis as the "appropriate Te supply condition", for example 400 mg of Te powder and 550 °C (vapor temperature of Te) in our previous report.[21] The "excessive Te supply condition" is defined as a Te powder quantity ranging from 0.5 to 1 g and a vapor temperature of 700 °C.

Under an excess Te supply, etching dominates. Cr_5Te_8 nanosheets undergo anisotropic etching, resulting in well-defined etched patterns characterized by triangular and hexagonal holes. Excess Te likely etches Cr_5Te_8 flakes by reacting with Cr atoms to create low-melting-point Cr–Te compounds, which then detach from the carrier gas. Although no similar anisotropic etching effect with excess chalcogen precursors has been reported in self-intercalated materials, a similar etching structure was observed in the CVD growth of MoS_2 with excess sulfur, which changed edge lengths and morphological structures.[36] Conversely, under an appropriate Te supply, unetched Cr_5Te_8 nanosheets are formed.[21] Typical

https://doi.org/10.1021/acs.cgd.5c00094
Cryst. Growth Des. XXXX, XXX, XXX–XXX

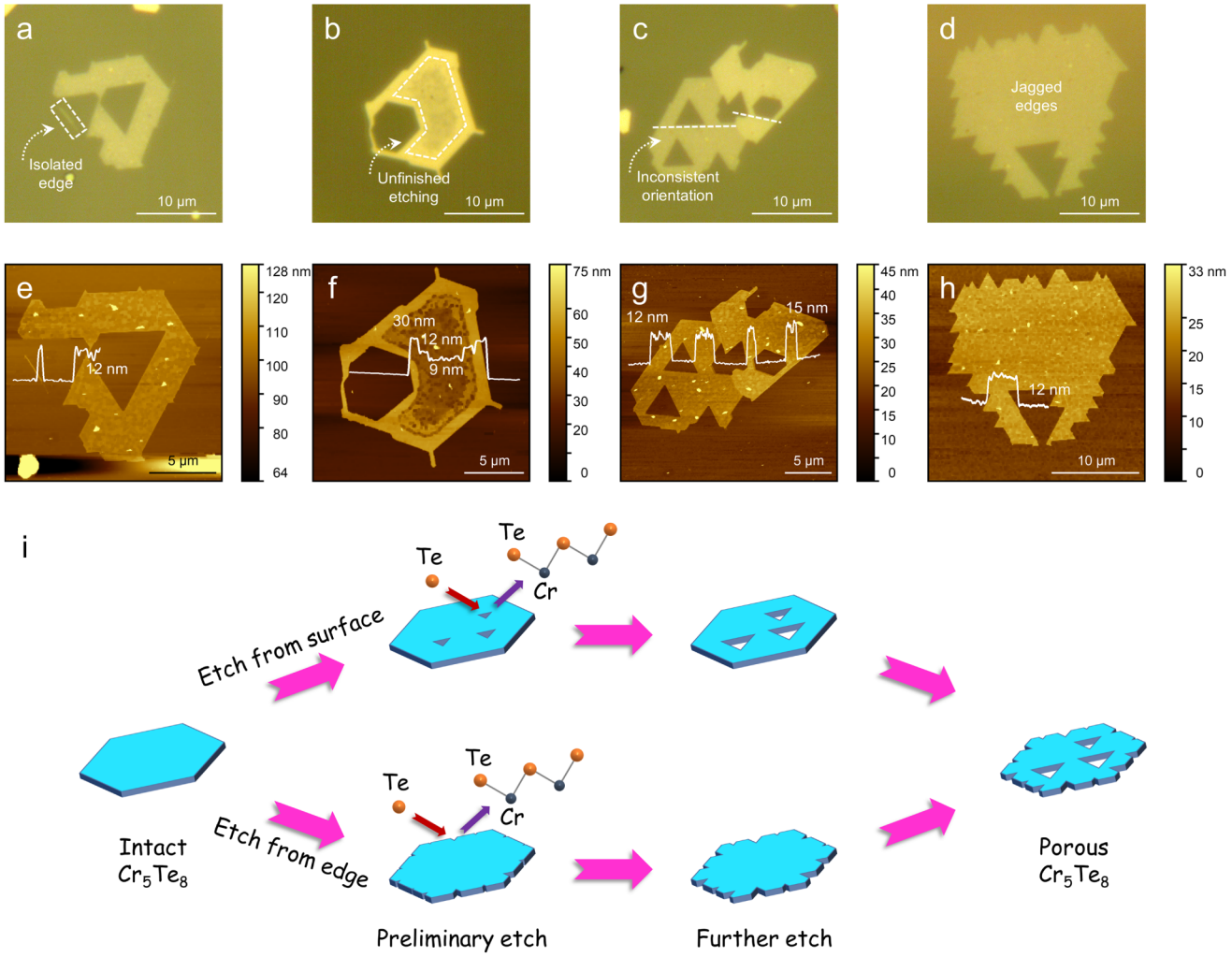

Figure 3. Etching mechanism of Cr_5Te_8. (a–d) OM images of Cr_5Te_8 with distinctive etching patterns. (e–h) AFM topographies corresponding to (a–d). (i) Schematic diagram of two etching pathways in Cr_5Te_8: initiating from the surface and initiating from the edge.

OM images of etched Cr_5Te_8 and pristine Cr_5Te_8 are presented in Figure 1b,c, respectively.[21]

To further verify the anisotropic etching of Cr_5Te_8 nanosheets, AFM characterization was employed on the etched Cr_5Te_8. Typical AFM topographies of 2D Cr_5Te_8 with etched patterns are presented in Figure 1d–g. The etched hole patterns exhibit directional triangular or hexagonal shapes with the hole edges aligned with the nanosheet edges. These distinct hole geometries directly validate the anisotropic nature of the etching process. Figure 1d–f depicts etched Cr_5Te_8 with varying hole densities. These topographies indicate that the nanosheet thicknesses are between 9 and 12 nm. Additionally, line profiles clearly confirm the formation of holes after the etching of Cr_5Te_8. Furthermore, the etching is related to the amount of Te. When the amount of Te increases, the etching effect is enhanced. The 1 g Te precursor results in more extensive etching of Cr_5Te_8. Figure 1g illustrates hexagonal ring-shaped, 10 nm thick Cr_5Te_8 nanoribbons approximately 1.5 μm in length and 180 nm in width after deep etching.

To confirm the crystal structure and composition of Cr_5Te_8 with etched patterns, comprehensive characterizations were conducted after the etched Cr_5Te_8 on mica was transferred to SiO_2/Si substrates to eliminate interference from the mica . In Figure 2a, XRD diffraction peaks at 14.4°, 29.3°, and 61.5° correspond to the (002), (004), and (008) diffraction planes, consistent with the standard PDF card of Cr_5Te_8 (PDF#50-1153).[28,29] This alignment affirms the structural accuracy of the as-grown 2D Cr_5Te_8 with etched patterns. Only (00X) peaks are observed in the XRD pattern, indicating that the surface of the etched Cr_5Te_8 is parallel to the *ab*-plane. The XPS spectrum exhibits binding energy peaks at 576.39 eV (Cr $2p_{3/2}$), 586.09 eV (Cr $2p_{1/2}$), 571.98 eV (Te $3d_{5/2}$), and 582.28 eV (Te $3d_{3/2}$), as shown in Figure 2b. These peaks indicate $Cr^{3.2+}$ and Te^{2-} states, determined using the charge potential model (CPM) and referencing standard data from the XPS handbook, which align with the valence states of Cr_5Te_8 crystals.[21,22]

EDS analysis of etched Cr_5Te_8 reveals an atomic ratio of Cr to Te approximately equal to 4.96:8, in good agreement with the stoichiometric ratio of Cr_5Te_8, as shown in Figure 2c. The SEM image and corresponding EDS mappings (Figure 2d–g) show clear contrasts between darkened holes and brightened nanosheets, confirming the formation of etched holes. The uniform color distribution of the nanosheets indicates the spatial uniformity of Cr and Te components, affirming the high quality of the etched Cr_5Te_8. Raman spectrum analysis on an individual Cr_5Te_8 nanosheet with etched patterns, as shown in

https://doi.org/10.1021/acs.cgd.5c00094
Cryst. Growth Des. XXXX, XXX, XXX−XXX

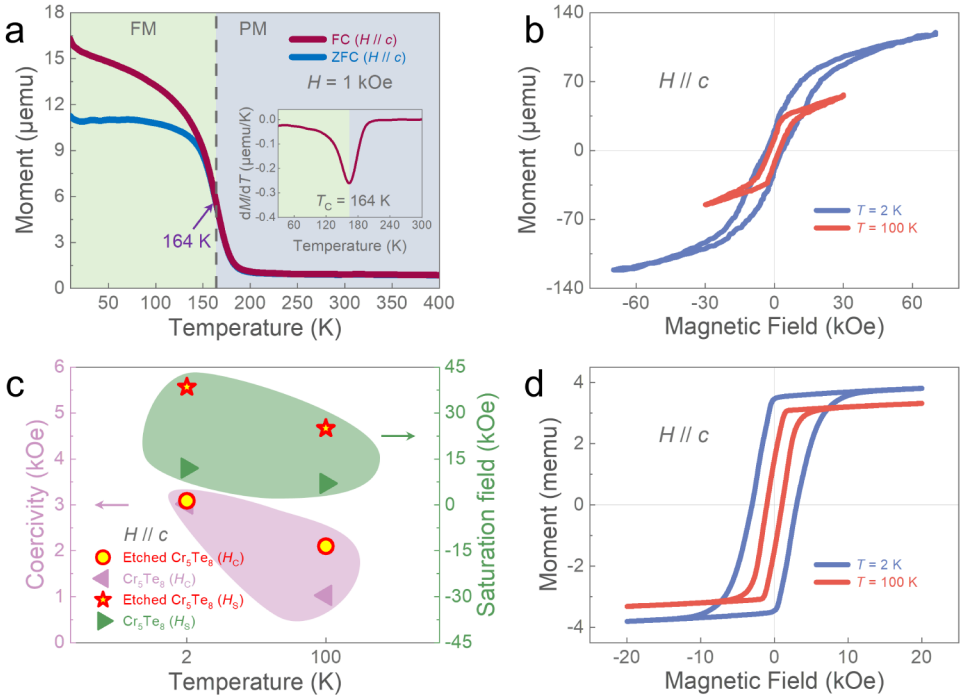

Figure 4. Ferromagnetism of the etched-pattern Cr_5Te_8. (a) $M-T$ curves of both the FC process (red line) and ZFC process (blue line) under an external field of 1 kOe perpendicular to the *ab*-plane. The inset displays the first-order derivative of M with respect to T to determine the T_C of etched Cr_5Te_8. (b, d) $M-H$ curves of etched Cr_5Te_8 (b) and intact Cr_5Te_8 (d) with the magnetic field perpendicular to the *ab*-plane at different temperatures. (c) Temperature-dependent coercivity and saturation field for etched Cr_5Te_8 and intact Cr_5Te_8 with the magnetic field perpendicular to the *ab*-plane.

Figure 2h, displays prominent peaks at 125 cm^{-1} and 140 cm^{-1}, corresponding to A_{1g} and E_g modes,[21−26] further confirming the crystallinity of etched Cr_5Te_8. As shown in Figure 2i,j, the OM image and corresponding Raman mappings provide additional evidence of the presence of holes in the Cr_5Te_8 nanosheets.

Furthermore, the unetched Cr_5Te_8 nanosheets were reported in our previous work,[21] and their composition and structural characteristics are identical to those of the etched nanosheets. Therefore, we conclude that the only difference between etched and unetched Cr_5Te_8 lies in the morphology, with the etched samples exhibiting no detectable defect states within the resolution of our measurements. In summary, the etched Cr_5Te_8 nanosheets retain the same quality, precise composition, and crystal structure as the unetched Cr_5Te_8. These findings provide an excellent opportunity for further investigations into the etching mechanism and its impact on the 2D magnetism of Cr_5Te_8.

To investigate the etching mechanism of Cr_5Te_8, we performed OM and AFM measurements on additional Cr_5Te_8 nanosheets with etched patterns on mica. Figure 3a−d presents OM images of Cr_5Te_8 with distinctly different etching patterns. The corresponding AFM topographies are shown in Figure 3e−h. In Figure 3a,e, the etching leaves an isolated-edge structure on Cr_5Te_8, indicating that the holes are indeed formed through etching rather than by separately assembling different Cr_5Te_8 molecules. Figure 3b,f shows the etched Cr_5Te_8 nanosheets with multiple "steps", suggesting that the etching process can start from the center of the nanosheet and gradually propagate outward. In Figure 3c,g, two Cr_5Te_8 nanosheets with different orientations are merged, and each hole's edge is parallel to the edge of its respective nanosheet. This orientation indicates that the anisotropy of the etched holes is only related to the crystal orientation of Cr_5Te_8. The shape of the etched Cr_5Te_8 nanosheet in Figure 3d,h is distinctly different from those shown in Figure 3a−c. The nanosheet's edge displays numerous serrations, suggesting that the etching process can initiate from both the surface and the edge of nanosheets. Additionally, in Figure 3a−h, various etched hole shapes, such as triangles and hexagons, are observed. These different etching patterns may result from the atomic termination differences at the hole edges, arising from the competition between the Te atom detachment rate and the Cr atom detachment rate during the etching process, similar to the etching of other 2D materials such as MoS_2, where triangular and hexagonal holes are characterized by edges terminated by different atoms.[37]

During the etching process of Cr_5Te_8, the freshly grown Cr_5Te_8 nanosheets undergo a desorption process in the presence of excess Te, leading to the formation of lower-melting-point Cr−Te compounds, which subsequently detach from the nanosheet. Two potential etching pathways have been identified. The etching model is illustrated in Figure 3i. The etching of an entire Cr_5Te_8 nanosheet can occur simultaneously along two pathways: the first involves the random formation of etching sites on the surface, followed by the etching gradually expanding outward along the crystal orientation of Cr_5Te_8 from these sites; the second pathway entails direct etching from the edge inward along the crystal orientation. The concurrent progression of etching along these two pathways results in the formation of Cr_5Te_8 with anisotropic hole patterns. Moreover, due to the higher atomic reactivity at the edge of Cr_5Te_8 nanosheets compared to the surface, it is more likely for etching sites to form at the edges. This is consistent with the higher hole density and deeper etching observed at the edges of the nanosheets in Figure 3a−

https://doi.org/10.1021/acs.cgd.5c00094
Cryst. Growth Des. XXXX, XXX, XXX−XXX

h, as well as the increased hole density at the corners of etched MoS_2 flakes compared to the central regions.[37] These findings provide crucial insights into the multifaceted etching behavior of Cr_5Te_8, revealing the intricate interplay between the etching processes and the crystal anisotropy of Cr_5Te_8.

To investigate the impact of etching on the magnetism of Cr_5Te_8 compared with that of pristine Cr_5Te_8, MPMS was used to measure the total magnetic signal of all etched nanosheets on mica. The ZFC and FC curves under an external field of 1 kOe perpendicular to the *ab*-plane are presented in Figure 4a. The magnetic moment decreases with increasing temperature until it disappears around 164 K, indicating the ferromagnetic order of etched Cr_5Te_8. Additionally, the first-order derivative of $M-T$ in the inset reveals a magnetic phase transition from paramagnetic to ferromagnetic at T_C = 164 K. The T_C of etched Cr_5Te_8 is slightly lower than the 176 K of unetched 2D Cr_5Te_8,[21] likely due to an increase in atomic defects induced by etching. Further confirmation of ferromagnetism was obtained from the $M-H$ curves. Figure 4b displays the $M-H$ curves at various temperatures under an external field perpendicular to the *ab*-plane. The ferromagnetism of etched Cr_5Te_8 is evident from the $M-H$ hysteresis loops at 2 and 100 K. Interestingly, the ferromagnetism of etched Cr_5Te_8 is temperature-sensitive, indicated by the shrinking size of hysteresis loops with increasing temperature. Notably, the saturated magnetic field of etched Cr_5Te_8 is significantly enhanced compared to that of pristine Cr_5Te_8. At 2 K, the saturated magnetic field for etched Cr_5Te_8 is considerably increased to 38.5 kOe, while pristine Cr_5Te_8 under the same testing conditions exhibits a saturated magnetic field of only 12 kOe, as shown in Figure 4d.[21] Additionally, the coercivity of etched Cr_5Te_8 is also enhanced compared to that of pristine Cr_5Te_8. The comparison of the coercivity and saturation field between etched Cr_5Te_8 and pristine Cr_5Te_8 at different temperatures is depicted in Figure 4c.

The increased coercivity and saturated magnetic field in etched Cr_5Te_8 may arise from the larger edge-to-area ratio, which strengthens the reentrant stray field of the saturated magnetic domains. For unetched 2D Cr_5Te_8 nanosheets, labyrinthine magnetic domains spontaneously form in the absence of external fields below the T_C. Upon increasing the applied magnetic field, these domains progressively transition into saturated single domains. At magnetic saturation, a reentrant stray field emerges externally, with maximal magnetic signal intensity observed at the nanosheet edges, where discontinuities in magnetization and thickness occur, contrasting sharply with minimal signals in central regions.[21] This magnetic configuration bears striking similarity to cleaved $CrCl_3$ flakes.[38] Their MFM studies revealed inhomogeneous single-domain states under saturating fields, characterized by attractive magnetic interactions within the flake interiors and repulsive forces along the peripheries. These observations confirm perpendicular magnetization alignment under external fields, generating reentrant stray fields that peak at structural discontinuities (e.g., edges) while diminishing in uniform bulk regions, analogous to the theoretical prediction that infinite magnetic planes produce no stray fields.[39]

Building upon this framework, we propose that the etched holes in Cr_5Te_8 nanosheets fundamentally alter the magnetic configuration by increasing the edge-to-area ratio. This geometric modification amplifies reentrant stray field contributions through two mechanisms: (i) introducing additional magnetization discontinuity sites at hole peripheries and (ii) fragmenting the nanosheet into smaller effective domains. Consequently, higher external magnetic fields become necessary to overcome the intensified stray field interactions and achieve full magnetization saturation. Similar magnetic behavior also appeared in etched MoS_2, where the increasing edge length resulted in a higher total magnetic moment and significantly enhanced saturation magnetization than that of unetched flakes.[37] Although a quantitative comparison of the saturation magnetization is difficult due to variations in nanosheet coverage across the substrate, our experiments clearly show significant enhancement in the coercivity and saturated magnetic field of the etched nanosheets. The significantly increased saturated magnetic field in etched Cr_5Te_8 provides a new perspective for controlling the magnetism of 2D materials and studying the evolution mechanism of magnetic domains in 2D materials.

CONCLUSIONS

In conclusion, we have studied the anisotropic etching process of Cr_5Te_8 nanosheets. Cr_5Te_8 nanosheets exhibiting various etched hole patterns, including triangular and hexagonal shapes, were successfully synthesized under excess Te precursor by the CVD method. To the best of our knowledge, this is the first report of anisotropic etching in 2D Cr_5Te_8. By tuning the amount of Te precursors, Cr_5Te_8 nanosheets were etched into nanoribbons. The etching process of Cr_5Te_8 nanosheets involves two pathways: initiation from the surface and from the edge. Remarkably, the etched Cr_5Te_8 nanosheets exhibit an enhanced saturated magnetic field, which is up to 3.2 times that of the intact nanosheets and is likely attributed to the increased edge proportion, which strengthens the reentrant stray field of the saturated magnetic domains. This investigation offers critical insights into the multifaceted etching behavior of Cr_5Te_8, unveiling a novel approach for manipulating the magnetism of 2D materials.

AUTHOR INFORMATION

Corresponding Author

Fei Pang − *Beijing Key Laboratory of Optoelectronic Functional Materials & Micro-nano Devices, School of Physics, Renmin University of China, Beijing 100872, China; Key Laboratory of Quantum State Construction and Manipulation (Ministry of Education), Renmin University of China, Beijing 100872, China;* orcid.org/0000-0002-8578-366X; Email: feipang@ruc.edu.cn

Authors

Hanxiang Wu − *Beijing Key Laboratory of Optoelectronic Functional Materials & Micro-nano Devices, School of Physics, Renmin University of China, Beijing 100872, China; Key Laboratory of Quantum State Construction and Manipulation (Ministry of Education), Renmin University of China, Beijing 100872, China*

Zuoquan Tan − *Beijing Key Laboratory of Optoelectronic Functional Materials & Micro-nano Devices, School of Physics, Renmin University of China, Beijing 100872, China; Key Laboratory of Quantum State Construction and Manipulation (Ministry of Education), Renmin University of China, Beijing 100872, China*

Zhaxi Suonan − *Beijing Key Laboratory of Optoelectronic Functional Materials & Micro-nano Devices, School of Physics, Renmin University of China, Beijing 100872, China; Key Laboratory of Quantum State Construction and*

https://doi.org/10.1021/acs.cgd.5c00094
Cryst. Growth Des. XXXX, XXX, XXX−XXX

Manipulation (Ministry of Education), Renmin University of China, Beijing 100872, China

Shanshan Chen − *Beijing Key Laboratory of Optoelectronic Functional Materials & Micro-nano Devices, School of Physics, Renmin University of China, Beijing 100872, China; Key Laboratory of Quantum State Construction and Manipulation (Ministry of Education), Renmin University of China, Beijing 100872, China;* orcid.org/0000-0002-3155-8571

Rui Xu − *Beijing Key Laboratory of Optoelectronic Functional Materials & Micro-nano Devices, School of Physics, Renmin University of China, Beijing 100872, China; Key Laboratory of Quantum State Construction and Manipulation (Ministry of Education), Renmin University of China, Beijing 100872, China*

Wei Ji − *Beijing Key Laboratory of Optoelectronic Functional Materials & Micro-nano Devices, School of Physics, Renmin University of China, Beijing 100872, China; Key Laboratory of Quantum State Construction and Manipulation (Ministry of Education), Renmin University of China, Beijing 100872, China;* orcid.org/0000-0001-5249-6624

Zhihai Cheng − *Beijing Key Laboratory of Optoelectronic Functional Materials & Micro-nano Devices, School of Physics, Renmin University of China, Beijing 100872, China; Key Laboratory of Quantum State Construction and Manipulation (Ministry of Education), Renmin University of China, Beijing 100872, China;* orcid.org/0000-0003-4938-4490

Complete contact information is available at: https://pubs.acs.org/10.1021/acs.cgd.5c00094

Notes

The authors declare no competing financial interest.

■ ACKNOWLEDGMENTS

This work was supported by the National Natural Science Foundation of China (Nos. 92477205, 12374200, 92477128, and 52461160327) and the Ministry of Science and Technology (MOST) of China (No. 2023YFA1406500). H.X.W. was supported by the Outstanding Innovative Talents Cultivation Funded Programs 2024 of Renmin University of China.

■ REFERENCES

(1) Akinwande, D.; Petrone, N.; Hone, J. Two-Dimensional Flexible Nanoelectronics. *Nat. Commun.* **2014**, *5*, 5678.

(2) Lin, Z.; Liu, Y.; Halim, U.; Ding, M.; Liu, Y.; Wang, Y.; Jia, C.; Chen, P.; Duan, X.; Wang, C.; Song, F.; Li, M.; Wan, C.; Huang, Y.; Duan, X. Solution-Processable 2D Semiconductors for High-Performance Large-Area Electronics. *Nature* **2018**, *562*, 254−258.

(3) Wang, Q. H.; Kalantar-Zadeh, K.; Kis, A.; Coleman, J. N.; Strano, M. S. Electronics and Optoelectronics of Two-Dimensional Transition Metal Dichalcogenides. *Nat. Nanotechnol.* **2012**, *7*, 699−712.

(4) Kim, E.; Lee, Y.; Ko, C.; Park, Y.; Yeo, J.; Chen, Y.; Choe, H. S.; Allen, F. I.; Rho, J.; Tongay, S. Tuning the Optical and Electrical Properties of MoS_2 by Selective Ag Photo-Reduction. *Appl. Phys. Lett.* **2018**, *113*, 013105.

(5) Hossain, M.; Qin, B.; Li, B.; Duan, X. S. Synthesis, characterization, properties and applications of two-dimensional magnetic materials. *Nano Today* **2022**, *42*, 101338.

(6) Klein, D. R.; MacNeill, D.; Lado, J. L.; Soriano, D.; Navarro-Moratalla, E.; Watanabe, K.; Taniguchi, T.; Manni, S.; Canfield, P.; Fernandez-Rossier, J.; Jarillo-Herrero, P. Probing Magnetism in 2D van der Waals Crystalline Insulators via Electron Tunneling. *Science* **2018**, *360*, 1218−1222.

(7) Huang, B.; Clark, G.; Navarro-Moratalla, E.; Klein, D. R.; Cheng, R.; Seyler, K. L.; Zhong, D.; Schmidgall, E.; McGuire, M. A.; Cobden, D. H.; Yao, W.; Xiao, D.; Jarillo-Herrero, P.; Xu, X. Layer-Dependent Ferromagnetism in a van der Waals Crystal Down to the Monolayer Limit. *Nature* **2017**, *546*, 270−273.

(8) Meng, L.; Zhou, Z.; Xu, M.; Yang, S.; Si, K.; Liu, L.; Wang, X.; Jiang, H.; Li, B.; Qin, P.; et al. Anomalous Thickness Dependence of Curie Temperature in Air-Stable Two-Dimensional Ferromagnetic 1T-$CrTe_2$ Grown by Chemical Vapor Deposition. *Nat. Commun.* **2021**, *12*, 809.

(9) Sun, X.; Li, W.; Wang, X.; Sui, Q.; Zhang, T.; Wang, Z.; Liu, L.; Li, D.; Feng, S.; Zhong, S.; Wang, H.; Bouchiat, V.; Nunez Regueiro, M.; Rougemaille, N.; Coraux, J.; Purbawati, A.; Hadj-Azzem, A.; Wang, Z.; Dong, B.; Wu, X.; et al. Room Temperature Ferromagnetism in Ultra-Thin van der Waals Crystals of 1T-$CrTe_2$. *Nano Res.* **2020**, *13*, 3358−3363.

(10) Wu, H.; Zhang, W.; Yang, L.; Wang, J.; Li, J.; Li, L.; Gao, Y.; Zhang, L.; Du, J.; Shu, H.; et al. Strong Intrinsic Room-Temperature Ferromagnetism in Freestanding Non−van der Waals Ultrathin 2D Crystals. *Nat. Commun.* **2021**, *12*, 5688.

(11) Wang, M.; Kang, L.; Su, J.; Zhang, L.; Dai, H.; Cheng, H.; Han, X.; Zhai, T.; Liu, Z.; Han, J. Two-Dimensional Ferromagnetism in CrTe Flakes Down to Atomically Thin Layers. *Nanoscale* **2020**, *12*, 16427−16432.

(12) Coughlin, A. L.; Xie, D.; Yao, Y.; Zhan, X.; Chen, Q.; Hewa-Walpitage, H.; Zhang, X.; Guo, H.; Zhou, H.; Lou, J.; Wang, J.; Li, Y. S.; Fertig, H. A.; Zhang, S. Near Degeneracy of Magnetic Phases in Two-Dimensional Chromium Telluride with Enhanced Perpendicular Magnetic Anisotropy. *ACS Nano* **2020**, *14*, 15256−15266.

(13) Roy, A.; Guchhait, S.; Dey, R.; Pramanik, T.; Hsieh, C. C.; Rai, A.; Banerjee, S. K. Perpendicular Magnetic Anisotropy and Spin Glass-Like Behavior in Molecular Beam Epitaxy Grown Chromium Telluride Thin Films. *ACS Nano* **2015**, *9*, 3772−3779.

(14) Li, H.; Wang, L.; Chen, J.; Yu, T.; Zhou, L.; Qiu, Y.; He, H.; Ye, F.; Sou, I. K.; Wang, G. Molecular Beam Epitaxy Grown Cr_2Te_3 Thin Films with Tunable Curie Temperatures for Spintronic Devices. *ACS Appl. Nano Mater.* **2019**, *2*, 6809−6817.

(15) Bian, M.; Kamenskii, A. N.; Han, M.; Li, W.; Wei, S.; Tian, X.; Eason, D. B.; Sun, F.; He, K.; Hui, H.; Yao, F.; Sabirianov, R.; Bird, J. P.; Yang, C.; Miao, J.; Lin, J.; Crooker, S. A.; Hou, Y.; Zeng, H. Covalent 2D Cr_2Te_3 Ferromagnet. *Mater. Res. Lett.* **2021**, *9*, 205−212.

(16) Zhong, J.; Wang, M.; Liu, T.; Zhao, Y.; Xu, X.; Zhou, S.; Han, J.; Gan, L.; Zhai, T. Strain-Sensitive Ferromagnetic Two-Dimensional Cr_2Te_3. *Nano Res.* **2022**, *15*, 1254−1259.

(17) Wen, Y.; Liu, Z.; Zhang, Y.; Xia, C.; Zhai, B.; Zhang, X.; Zhai, G.; Shen, C.; He, P.; Cheng, R.; Yin, L.; Yao, Y.; Getaye Sendeku, M.; Wang, Z.; Ye, X.; Liu, C.; Jiang, C.; Shan, C.; Long, Y.; He, J. Tunable Room-Temperature Ferromagnetism in Two-Dimensional Cr_2Te_3. *Nano Lett.* **2020**, *20*, 3130−3139.

(18) Guo, Y.; Kang, L.; Yu, S.; Yang, J.; Qi, X.; Zhang, Z.; Liu, Z. CVD Growth of Large-Scale and Highly Crystalline 2D Chromium Telluride Nanoflakes. *ChemNanomater* **2021**, *7*, 323−327.

(19) Coughlin, A. L.; Xie, D.; Zhan, X.; Yao, Y.; Deng, L.; Hewa-Walpitage, H.; Bontke, T.; Chu, C. W.; Li, Y.; Wang, J.; Fertig, H. A.; Zhang, S. van der Waals Superstructure and Twisting in Self-Intercalated Magnet with Near Room-Temperature Perpendicular Ferromagnetism. *Nano Lett.* **2021**, *21*, 9517−9525.

(20) Wang, W.; Fan, J.; Liu, H.; Zheng, H.; Ma, C.; Zhang, L.; Sun, Y.; Wang, C.; Zhu, Y.; Yang, H. Fabrication and Magnetic-Electronic Properties of van der Waals Cr_4Te_5 Ferromagnetic Films. *CrystEngcomm* **2022**, *24*, 674−680.

(21) Wu, H.; Guo, J.; Zhaxi, S.; Xu, H.; Mi, S.; Wang, L.; Chen, S.; Xu, R.; Ji, W.; Pang, F.; Cheng, Z. Controllable CVD Growth of 2D Cr_5Te_8 Nanosheets with Thickness-Dependent Magnetic Domains. *ACS Appl. Mater. Interfaces* **2023**, *15*, 26148−26158.

(22) Chen, C.; Chen, X.; Wu, C.; Wang, X.; Ping, Y.; Wei, X.; Zhou, X.; Lu, J.; Zhu, L.; Zhou, J.; et al. Air-Stable 2D Cr_5Te_8 Nanosheets

with Thickness-Tunable Ferromagnetism. *Adv. Mater.* **2022**, *34*, 2107512.
(23) Jin, Z.; Ji, Z.; Zhong, Y.; Jin, Y.; Hu, X.; Zhang, X.; Zhu, L.; Huang, X.; Li, T.; Cai, X.; Zhou, L. Controlled Synthesis of a Two-Dimensional Non-van der Waals Ferromagnet toward a Magnetic Moiré Superlattice. *ACS Nano* **2022**, *16*, 7572−7579.
(24) Bian, M.; Zhu, L.; Wang, X.; Choi, J.; Chopdekar, R. V.; Wei, S.; Wu, L.; Huai, C.; Marga, A.; Yang, Q.; et al. Dative Epitaxy of Commensurate Monocrystalline Covalent van der Waals Moiré Supercrystal. *Adv. Mater.* **2022**, *34*, 2200117.
(25) Tang, B.; Wang, X.; Han, M.; Xu, X.; Zhang, Z.; Zhu, C.; Cao, X.; Yang, Y.; Fu, Q.; Yang, J.; Li, X.; Gao, W.; Zhou, J.; Lin, J.; Liu, Z. Phase Engineering of Cr_5Te_8 with Colossal Anomalous Hall Effect. *Nat. Electron.* **2022**, *5*, 224−232.
(26) Niu, K.; Qiu, G.; Wang, C.; Li, D.; Niu, Y.; Li, S.; Kang, L.; Cai, Y.; Han, M.; Lin, J. Self-Intercalated Magnetic Heterostructures in 2D Chromium Telluride. *Adv. Funct. Mater.* **2023**, *33*, 2208528.
(27) Huang, Z.-L.; Kockelmann, W.; Telling, M.; Bensch, W. A Neutron Diffraction Study of Structural and Magnetic Properties of Monoclinic Cr_5Te_8. *Solid State Sci.* **2008**, *10*, 1099−1105.
(28) Lukoschus, K.; Kraschinski, S.; Näther, C.; Bensch, W.; Kremer, R. K. Magnetic Properties and Low Temperature X-Ray Studies of the Weak Ferromagnetic Monoclinic and Trigonal Chromium Tellurides Cr_5Te_8. *J. Solid State Chem.* **2004**, *177*, 951−959.
(29) Zhang, X.; Yu, T.; Xue, Q.; Lei, M.; Jiao, R. Critical Behavior and Magnetocaloric Effect in Monoclinic Cr_5Te_8. *J. Alloys Compd.* **2018**, *750*, 798−803.
(30) Li, X.; Dong, J.; Idrobo, J. C.; Puretzky, A. A.; Rouleau, C. M.; Geohegan, D. B.; Ding, F.; Xiao, K. Edge-Controlled Growth and Etching of Two-Dimensional GaSe Monolayers. *J. Am. Chem. Soc.* **2017**, *139*, 482−491.
(31) Kong, X.; Fu, C.; Gladkikh, V.; Ding, F. The Shapes of Synthesized Two-Dimensional Materials. *Smartmat* **2023**, *4*, No. e1152.
(32) Zhang, Q.; He, W.; Li, L.; Geng, D.; Xu, Z.; Chen, H.; Chen, W.; Hu, W. Oxygen-Assisted Anisotropic Chemical Etching of $MoSe_2$ for Enhanced Phototransistors. *Chem. Mater.* **2022**, *34*, 4212−4223.
(33) Sun, H.; Dong, J.; Liu, F.; Ding, F. Etching of Two-Dimensional Materials. *Mater. Today* **2021**, *42*, 192−213.
(34) Zhang, Y.; Li, Z.; Kim, P.; Zhang, L.; Zhou, C. Anisotropic Hydrogen Etching of Chemical Vapor Deposited Graphene. *ACS Nano* **2012**, *6*, 126−132.
(35) Stehle, Y. Y.; Sang, X.; Unocic, R. R.; Voylov, D.; Jackson, R. K.; Smirnov, S.; Vlassiouk, I. Anisotropic Etching of Hexagonal Boron Nitride and Graphene: Question of Edge Terminations. *Nano Lett.* **2017**, *17*, 7306−7314.
(36) Chen, F.; Jiang, X.; Shao, J.; Lu, B.; Fu, L.; Zhao, S.; Su, W. Space-Confined CVD Growth of 2D-MoS_2 Crystals with Tunable Dimensionality via Adjusting Growth Conditions. *CrystEngcomm* **2021**, *23*, 1345−1351.
(37) Li, Q.; Luo, Q.; Zhu, Y.; Zheng, B.; Zhou, L.; Chen, F.; Wu, D.; Peng, R.-W.; Wang, M. Anisotropic Etching of Monolayer MoS_2 Flakes for Zigzag Edges in Chemical Vapor Deposition. *ACS Appl. Mater. Interfaces* **2024**, *16*, 66792−66801.
(38) Serri, M.; Cucinotta, G.; Poggini, L.; Serrano, G.; Sainctavit, P.; Strychalska-Nowak, J.; Politano, A.; Bonaccorso, F.; Caneschi, A.; Cava, R. J.; et al. Enhancement of the Magnetic Coupling in Exfoliated $CrCl_3$ Crystals Observed by Low-Temperature Magnetic Force Microscopy and X-Ray Magnetic Circular Dichroism. *Adv. Mater.* **2020**, *32*, 2000566.
(39) Van Schendel, P. J. A.; Hug, H. J.; Stiefel, B.; Martin, S.; Guntherodt, H. J. A Method for the Calibration of Magnetic Force Microscopy Tips. *J. Appl. Phys.* **2000**, *88*, 435−445.

https://doi.org/10.1021/acs.cgd.5c00094
Cryst. Growth Des. XXXX, XXX, XXX−XXX